

Asteroseismology of red giants

By Jørgen Christensen-Dalsgaard¹

¹Department of Physics and Astronomy, Building 1520, Aarhus University, Ny Munkegade,
8000 Aarhus C, Denmark

Red-giant stars are emerging as one of the most interesting areas of space asteroseismology. Even a relatively basic analysis leads to the determination of the global parameters of the stars, such as their mass and radius, and the very extensive space-based data now available for a large number of stars allow detailed investigation of the deep interiors of red giants, including distinguishing between stars that do and do not have helium fusion in the core, on the basis of periods of gravity waves partially trapped in the core. Here I review the theoretical background for these new developments and provide a simple explanation for the effect on the period spacing of central helium fusion.

1. Introduction

Asteroseismology, and hence the study of stellar properties, is being revolutionized by the extremely accurate and extensive data from the CoRoT (Baglin et al. 2009) and *Kepler* (Borucki et al. 2009) space missions. Analysis of timeseries of unprecedented extent, continuity and sensitivity have allowed the study of a broad range of stellar variability, including oscillations of a variety of pulsating stars (see, e.g., Gilliland et al. 2010; Christensen-Dalsgaard & Thompson 2011, for reviews), and leading to comparative asteroseismology (or *synasteroseismology*[†]) for main-sequence stars showing solar-like oscillation (Chaplin et al. 2011). Also, early analyses of *Kepler* data have demonstrated the power of asteroseismology in characterizing the central stars in planetary systems (Christensen-Dalsgaard et al. 2010; Batalha et al. 2011), and such investigations will undoubtedly play a major role in the continuing *Kepler* exploration of extra-solar planetary systems.

However, perhaps the most striking results of space asteroseismology have come from the investigation of red giants. Given the extensive outer convection zones of red giants, solar-like oscillations were predicted quite early (Christensen-Dalsgaard & Frandsen 1983). Ground-based observations have been carried out in a few cases (e.g., Frandsen et al. 2002; De Ridder et al. 2006) but owing to the very long periods of these huge stars such observations are extremely demanding in terms of observing and observer's time. Space observations, on the other hand, allow nearly continuous observations over very extended periods, as demonstrated by early observations by the WIRE (Retter et al. 2003) and MOST (Barban et al. 2007) satellites. With CoRoT and *Kepler* we have obtained extensive data for literally thousands of red giants, providing precise characterization of their overall characteristics, as well as, in some cases, detailed information on the properties of their deep interiors. This promises completely to change our understanding of these late phases of stellar evolution.

Here I provide an overview of the oscillation properties of red giants and discuss some of the initial results of the analysis of data from CoRoT and *Kepler*. An introduction to the properties of solar-like oscillations, emphasizing the observational aspects, was provided by Bedding (this volume). Further introductions to solar-like stellar oscillations were provided by Christensen-Dalsgaard (2004) and, in particular, by the monograph

[†] a term coined by D. O. Gough

by Aerts et al. (2010). To illustrate the relevant properties, computations of red-giant models and oscillations are presented. These probably do not fully cover the complexities of these late stages of stellar evolution and hence are not intended as models of specific observations, but it is hoped that they at least capture the main features of these stars. The modelling was carried out using the Aarhus STellar Evolution Code ASTEC (Christensen-Dalsgaard 2008a), with OPAL equation of state (Rogers et al. 1996) and opacities (Iglesias & Rogers 1996), and NACRE (Angulo et al. 1999) nuclear reaction rates. Convection was treated with the Böhm-Vitense (1958) mixing-length formalism, with a mixing length proportional to the pressure scale height and approximately calibrated to a solar model. Diffusion and settling were neglected and no mass loss was included. Adiabatic oscillations were calculated using the Aarhus adiabatic pulsation code ADIPLS (Christensen-Dalsgaard 2008b). To resolve the very rapid variations in the eigenfunctions in the stellar core, the models were transferred from the original mesh used in the model calculation to a much finer mesh, designed to capture adequately the properties of the eigenfunctions. However, it is probably fair to say that the mesh distribution, and more generally the numerical procedures to deal with this type of oscillation, requires further optimization and testing.

2. Simple properties of stellar oscillations

This section provides a brief background on the theory of stellar oscillations, as far as the oscillation frequencies and their relation to stellar properties are concerned. Some emphasis is given to the oscillation properties of red giants.

To understand the properties of stellar oscillation frequencies, it is a good approximation to assume that the oscillations are adiabatic, and hence ignore the processes that damp or excite the modes. This approximation breaks down in the near-surface layers, where there are strong departures from adiabaticity. Also, the modelling of this region is highly uncertain, owing to the detailed effects of convection on the mean structure of the star and the dynamics of the oscillations. These near-surface processes have a significant effect on the frequencies, as is evident in the analysis of solar observations, and they must be taken into account in detailed asteroseismic analyses of solar-like oscillation frequencies (e.g., Kjeldsen et al. 2008). However, for the present discussion we can ignore them.

With this approximation the problem of computing stellar oscillation frequencies for a given stellar model is relatively straightforward.[†] This feature, together with the ability to determine the observed frequencies with very high accuracy, makes stellar oscillations such excellent diagnostics of the stellar interior. For the purpose of computing adiabatic frequencies, and assuming that the equilibrium model satisfies hydrostatic equilibrium (see Kewaler, this volume), the structure of the star is characterized by the density $\rho(r)$ as a function of distance r to the centre, as well as the adiabatic exponent $\Gamma_1(r)$, where

$$\Gamma_1 = \left(\frac{\partial \ln p}{\partial \ln \rho} \right)_{\text{ad}}, \quad (2.1)$$

where p is pressure and the derivative corresponds to an adiabatic change. Given $\rho(r)$ the mass distribution in the star can immediately be determined, and $p(r)$ can then be computed from the equation of hydrostatic equilibrium, with a suitable boundary condition. This essentially defines all that is needed to compute the equations of adiabatic oscillation. For the predominantly acoustic solar-like oscillations the most important

[†] Although, as discussed below some care is needed when considering red giants.

quantity is the adiabatic sound speed c , given by

$$c^2 = \frac{\Gamma_1 p}{\rho} . \quad (2.2)$$

In many relevant cases, the equation of state can be approximated by the ideal gas law:

$$p = \frac{k_B \rho T}{\mu m_u} , \quad (2.3)$$

where T is temperature, μ the mean molecular weight, k_B Boltzmann's constant and m_u the atomic mass unit. We then obtain

$$c^2 \simeq \frac{\Gamma_1 k_B T}{\mu m_u} . \quad (2.4)$$

We consider small-amplitude oscillations in a slowly rotating star. Then the dependence of the eigenfunctions on co-latitude θ and longitude ϕ can be separated as spherical harmonics $Y_l^m(\theta, \phi)$; the degree l measures the total number of nodal lines on the stellar surface and provides a measure of the local horizontal wavenumber k_h :

$$k_h^2 = \frac{l(l+1)}{r^2} , \quad (2.5)$$

while the azimuthal order m , with $|m| \leq l$, measures the number of nodal lines crossing the equator. For each (l, m) the star has a set of eigenfrequencies ω_{nlm} labelled by the radial order n . For adiabatic oscillations ω_{nlm} is real; the oscillation depends on time t and ϕ as $\cos(m\phi - \omega t)$, i.e., for $m \neq 0$, as a running wave in longitude. For a nonrotating star the frequencies are independent of m . Slow rotation with angular velocity Ω introduces a frequency splitting

$$\omega_{nlm} = \omega_{nl0} + m\beta_{nlm}\langle\Omega\rangle_{nlm} , \quad (2.6)$$

where $\langle\Omega\rangle_{nlm}$ is an average over the star with a weight determined by the oscillation eigenfunction. If $\omega = \Omega(r)$ depends on r alone $\beta_{nlm} = \beta_{nl}$ and the average are independent of m and the rotational splitting is linear in m .

After separation of Y_l^m the equations of adiabatic oscillations reduce to a set of four linear differential equations in r , which suitable boundary conditions at the centre and surface, which can be solved numerically, with the frequencies ω_{nlm} as eigenvalues. However, a great deal of insight into the properties of the solution and the relation of the frequencies to the structure of the star can be obtained from asymptotic analysis of the equations. Deubner & Gough (1984) derived an asymptotic equation, applicable for modes of high radial order, in terms of the quantity $X = c^2 \rho^{1/2} \text{div } \boldsymbol{\delta r}$, where $\boldsymbol{\delta r}$ is the displacement vector:

$$\frac{d^2 X}{dr^2} = -K(r)X , \quad (2.7)$$

where

$$K = \frac{1}{c^2} \left[S_l^2 \left(\frac{N^2}{\omega^2} - 1 \right) + \omega^2 - \omega_c^2 \right] . \quad (2.8)$$

Thus K is controlled by three characteristic frequencies of the star: the *Lamb frequency* S_l , with

$$S_l^2 = \frac{l(l+1)c^2}{r^2} , \quad (2.9)$$

the *buoyancy frequency* (or *Brunt-Väisälä frequency*) N ,

$$N^2 = g \left(\frac{1}{\Gamma_1} \frac{d \ln p}{dr} - \frac{d \ln \rho}{dr} \right), \quad (2.10)$$

where g is the local gravitational acceleration, and the *acoustic cut-off frequency* ω_c ,

$$\omega_c^2 = \frac{c^2}{4H^2} \left(1 - 2 \frac{dH}{dr} \right), \quad (2.11)$$

where $H = -(d \ln \rho / dr)^{-1}$ is the density scale height.

Equation (2.7) determines the local properties of the eigenfunction. In regions where $K(r) > 0$ the solution locally oscillates as a function of r , while the behaviour is exponentially increasing or decreasing where $K(r) < 0$. The intermediate points, where $K(r) = 0$, are called *turning points*. Often there is an interval $[r_1, r_2]$ where $K(r) > 0$, with K being negative just outside and the solution decreasing exponentially in the direction away from that interval. In that case the mode is said to be trapped between r_1 and r_2 ; from JWKB analysis (e.g., Gough 2007) one finds that the frequency approximately satisfies the dispersion relation

$$\int_{r_1}^{r_2} K^{1/2} dr = (n - 1/2)\pi. \quad (2.12)$$

The behaviour of the Lamb frequency and the acoustic cut-off frequency is relatively simple. The Lamb frequency generally decreases with increasing r ;† for the low degrees that are relevant to stellar observations it is small near the surface. Here, typically, ω_c^2 dominates in Eq. (2.8). In the atmosphere, where the temperature is approximately constant, H can be approximated by the (constant) pressure scale height and we obtain

$$\omega_c \simeq \omega_{c,\text{atm}} = \frac{1}{2} g \sqrt{\Gamma_1 \rho / p} \propto M R^{-2} T_{\text{eff}}^{-1/2}, \quad (2.13)$$

evaluated in the atmosphere; in the last proportionality we assumed the ideal gas law (see Eq. 2.3) and that the atmospheric temperature is proportional to the effective temperature T_{eff} . Below the surface ω_c decreases rapidly with increasing depth. When $\omega < \omega_{c,\text{atm}}$ the solution decreases with height in the atmosphere; this corresponds to reflection of the mode at the surface so that it is trapped in the stellar interior. Waves with $\omega > \omega_{c,\text{atm}}$ can propagate out through the atmosphere and hence lose energy, leading to strong damping. Thus $\omega_{c,\text{atm}}$ defines the upper limit in frequency to trapped modes, at least in the adiabatic approximation.

The behaviour of the buoyancy frequency is more complex. This is seen most clearly by assuming the ideal gas approximation, Eq. (2.3). Then we obtain, from Eq. (2.10), that

$$N^2 = g^2 \frac{\rho}{p} (\nabla_{\text{ad}} - \nabla + \nabla_\mu), \quad (2.14)$$

where, following the usual convention (see Kawaler, this volume),

$$\nabla = \frac{d \ln T}{d \ln p}, \quad \nabla_{\text{ad}} = \left(\frac{\partial \ln T}{\partial \ln p} \right)_{\text{ad}}, \quad \nabla_\mu = \frac{d \ln \mu}{d \ln p}. \quad (2.15)$$

Since typically μ increases towards the centre and hence with increasing p , as a result of nuclear burning, the term in ∇_μ typically gives a positive contribution to N^2 in the deep interior of the star. It should also be noted that the condition for convective instability‡

† possibly with the exception of discontinuities in composition, caused by nuclear burning in the stellar core, which leads to discontinuities in density and hence sound speed

‡ strictly speaking the Ledoux criterion

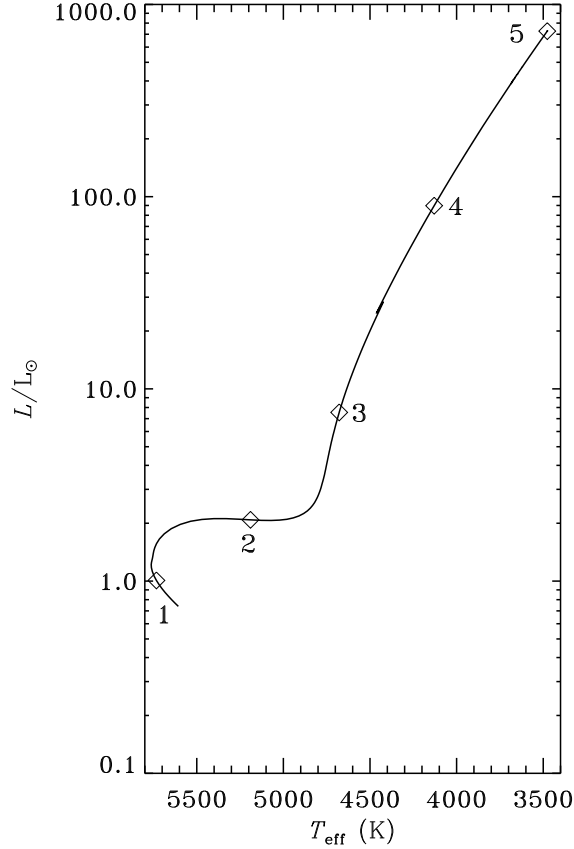


FIGURE 1. Evolution track for a $1M_{\odot}$ model, approximately calibrated to the Sun at the present solar age.

is that $N^2 < 0$. In convection zones the composition is uniform and $\nabla_{\mu} = 0$; also, except near the surface ∇ is nearly adiabatic and N^2 is only slightly negative.

Solar-like oscillations are believed to be excited stochastically by the vigorous motion in the near-surface layers of convective envelopes (see Section 3 below). Thus stars showing such oscillations have outer convection zones and hence the buoyancy frequency is positive only in the deeper interior. Here we illustrate the characteristic frequencies and their dependence on the evolutionary state by considering selected models in a $1 M_{\odot}$ evolution sequence, illustrated in an HR diagram in Fig. 1. A typical example of a rather unevolved star, at roughly solar age, is shown in Fig. 2. Here there is a fairly clear separation between S_l and N . As a result there are essentially two different scenarios for having a positive K , also illustrated in the figure: by having $\omega > S_l$ (and hence typically $\omega \gg N$) or by having $\omega < N$ (and hence typically $\omega \ll S_l$). The former case corresponds to acoustic modes (or p modes), where the restoring force is predominantly pressure, while the latter case corresponds to internal gravity waves (or g modes), where the restoring force is buoyancy.

In discussing the properties of these modes in more detail, we neglect ω_c in Eq. (2.8), except insofar as to use that it causes the required reflection at the surface of the p

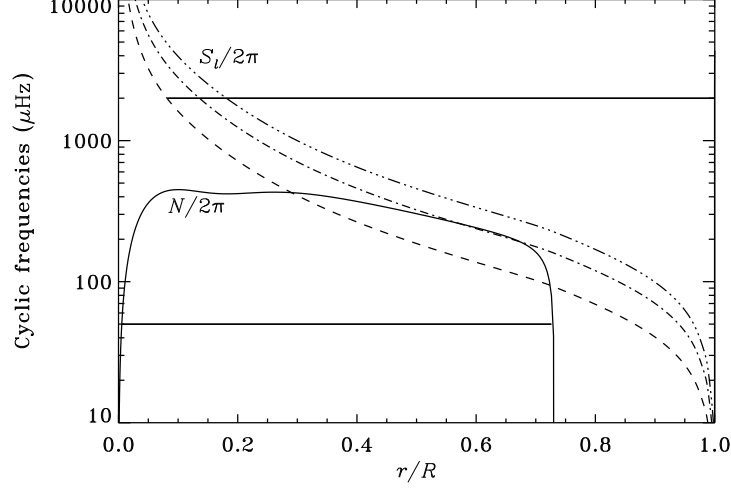


FIGURE 2. Characteristic cyclic frequencies for Model 1 in the $1M_{\odot}$ evolution sequence illustrated in Fig. 1. The solid curve shows $N/2\pi$, where N is the buoyancy frequency (cf. Eq. 2.10), whereas the dashed, dot-dashed and triple-dot-dashed curves show the Lamb frequency $S_l/2\pi$ (cf. Eq. 2.9) for $l = 1, 2$ and 3 , respectively. The horizontal solid lines show typical propagation regions for a p mode (with $l = 1$, at high frequency) and a g mode (at low frequency).

modes. For the p modes, assuming that $\omega \gg N$, we then obtain from Eq. (2.8) that

$$K \simeq \frac{1}{c^2}(\omega^2 - S_l^2), \quad (2.16)$$

with a lower turning point r_t defined by $S_l = \omega$ or

$$\frac{c(r_t)}{r_t} = \frac{\omega}{L}, \quad (2.17)$$

where $L^2 = l(l+1)$. Also, the corresponding approximation to Eq. (2.12) can be rearranged to yield

$$\int_{r_t}^R \left(1 - \frac{L^2 c^2}{r^2 \omega^2}\right)^{1/2} \frac{dr}{c} = \frac{(n + \alpha)\pi}{\omega}. \quad (2.18)$$

Here we replaced the $-1/2$ in Eq. (2.12) by α , which generally is a function of frequency, to account for the phase change in the reflection at the surface. Equation (2.18) has played a major role in the analysis of solar oscillation frequencies; a relation of this form was first obtained by Duvall (1982) from analysis of observed frequencies. It explicitly demonstrates that in this limit the frequencies are determined by the sound speed and by α .

In unevolved stars r_t is close to the centre where c varies relatively slowly. Equation (2.18) can then be expanded (Gough 1986, 1993) to yield, in terms of the cyclic frequencies $\nu_{nl} = \omega_{nl}/2\pi$,

$$\nu_{nl} = \Delta\nu \left(n + \frac{l}{2} + \alpha + \frac{1}{4} \right) - d_{nl}, \quad (2.19)$$

where

$$\Delta\nu = \left(2 \int_0^R \frac{dr}{c} \right)^{-1}, \quad (2.20)$$

and we replaced L by $l + 1/2$ (see also Vandakurov 1967; Tassoul 1980, 1990). Neglecting the small correction term d_{nl} this shows that the frequencies are uniformly spaced in radial order n , with a spacing given by the *large separation* $\Delta\nu$ and such that there is degeneracy between ν_{nl} and $\nu_{n-1, l+2}$. This degeneracy is lifted by d_{nl} which asymptotically, for main-sequence models, can be approximated by

$$d_{nl} \simeq -\frac{\Delta\nu}{4\pi^2\nu_{nl}} L^2 \int_0^R \frac{dc}{dr} \frac{dr}{r}. \quad (2.21)$$

To this approximation d_{nl} , and hence the small separations $\delta\nu_{l, l+2}(n) = \nu_{nl} - \nu_{n-1, l+2}$, are very sensitive to the sound-speed gradient in the stellar core and hence, according to Eq. (2.4), to the composition profile that has resulted from the nuclear burning. Thus for main-sequence stars the small frequency separations provide a measure of the evolutionary stage and hence the age of the star. Interestingly, although the derivation sketched above and the expression for d_{nl} do not hold for highly evolved stars such as red giants, the frequency pattern reflected in Eq. (2.19) is still found (see also Section 6).

In the opposite extreme, where $\omega \ll S_l$ and $\omega < N$, we approximate K by

$$K \simeq \frac{L^2}{r^2} \left(\frac{N^2}{\omega^2} - 1 \right). \quad (2.22)$$

With a relatively simple behaviour of N such as illustrated in Fig. 2 there are typically just two turning points r_1, r_2 where $\omega = N$, and Eq. (2.12) yields

$$L \int_{r_1}^{r_2} \left(\frac{N^2}{\omega^2} - 1 \right)^{1/2} \frac{dr}{r} = (n - 1/2)\pi. \quad (2.23)$$

If $\omega \ll N$ almost everywhere on $[r_1, r_2]$ we can approximate Eq. (2.23) further by neglecting 1 compared with N^2/ω^2 , to obtain finally an approximate expression for the period $\Pi = 2\pi/\omega$:

$$\Pi = \frac{\Pi_0}{L} (n + \alpha_g), \quad (2.24)$$

where

$$\Pi_0 = 2\pi^2 \left(\int_{r_1}^{r_2} N \frac{dr}{r} \right)^{-1}, \quad (2.25)$$

assuming that $N^2 \geq 0$ on $[r_1, r_2]$, with $N = 0$ at r_1 and r_2 (e.g., Tassoul 1980). Also, α_g , which may depend on l , reflects the actual phase shift at the turning points. Equation (2.24) shows that in this case we get periods that are uniformly spaced in the radial order n , with a spacing that is inversely proportional to L .

The dependence of the characteristic frequencies and hence the oscillation properties on stellar parameters can to a large extent be characterized by simple scaling relations. An important example is the scaling of the acoustic cut-off frequency in Eq. (2.13). Under many circumstances the structure of a star, as a function of the fractional radius $x = r/R$, approximately satisfies so-called *homology scaling relations* (e.g., Kippenhahn & Weigert 1990).[†] According to these pressure scales as GM^2/R^4 , G being the gravitational constant, and density scales as M/R^3 . It follows that the squared sound speed c^2 scales

[†] A simple example, where the scalings are exact, are polytropic models.

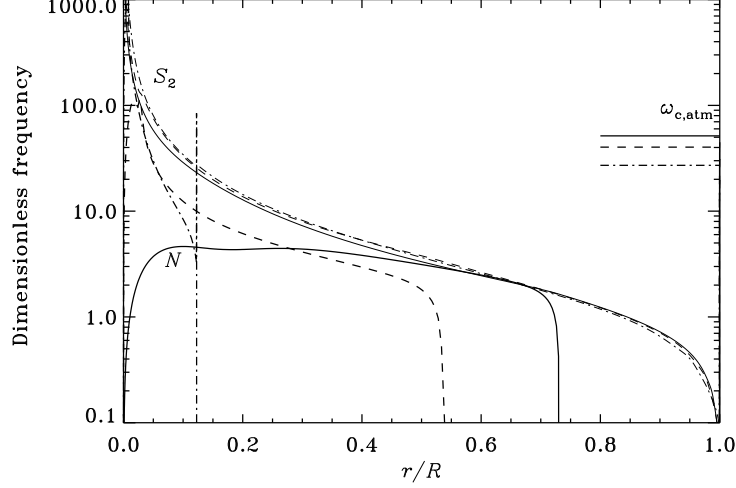


FIGURE 3. Dimensionless characteristic frequencies (in units of $(GM/R^3)^{1/2}$) for models along the $1M_{\odot}$ evolutionary track illustrated in Fig. 1. Solid, dashed and dot-dashed curves are for Models 1, 2 and 3, respectively. The thick curves show the buoyancy frequency N while the thinner curves show the Lamb frequency S_l , for $l = 2$. The horizontal lines at the right edge of the plot similarly show the dimensionless value of the acoustic cut-off frequency (cf. Eq. 2.13) in the atmosphere of the models.

as GM/R and the squared characteristic frequencies scale as GM/R^3 . This motivates introducing the dimensionless scaled frequencies by

$$\hat{S}_l^2 = \frac{R^3}{GM} S_l^2, \quad \hat{N}^2 = \frac{R^3}{GM} N^2, \quad \hat{\omega}_c^2 = \frac{R^3}{GM} \omega_c^2, \quad (2.26)$$

as well as $\hat{c}^2 = (R/GM)c^2$. Then the asymptotic equations (2.7) and (2.8) can be expressed as

$$\frac{d^2 X}{dx^2} = -\hat{K}(r)X, \quad (2.27)$$

where

$$\hat{K} = \frac{1}{\hat{c}^2} \left[\hat{S}_l^2 \left(\frac{\hat{N}^2}{\sigma^2} - 1 \right) + \sigma^2 - \hat{\omega}_c^2 \right], \quad (2.28)$$

in terms of the dimensionless frequency

$$\sigma^2 = \frac{R^3}{GM} \omega^2. \quad (2.29)$$

With similar scalings the full equations of adiabatic oscillations can be expressed in a form that is homologously invariant. It follows that homologous models have the same dimensionless frequencies σ_{nl} , and that the actual frequencies satisfy the scaling

$$\omega_{nl} \propto (M/R^3)^{1/2} \propto \langle \rho \rangle^{1/2}, \quad (2.30)$$

where $\langle \rho \rangle$ is the mean density of the star. The same scaling obviously applies, e.g., to the large frequency separation $\Delta\nu$.

Actual stellar models are never strictly homologous, and in particular the changing structure of the core as nuclear burning proceeds gives strong departures from these scalings. On the other hand, they are approximately satisfied in the outer layers which

predominantly determine the frequencies of acoustic modes, and hence for such modes the scaling in Eq. (2.30) is a reasonable approximation. To illustrate this we consider the evolution of the frequencies along a $1 M_{\odot}$ evolution sequence, illustrated in Fig. 1. The dimensionless frequencies for Models 1, 2 and 3 are shown in Fig. 3. Evidently there is relatively little change in \hat{S}_2 . On the other hand, the changes in \hat{N} are dramatic, showing very strong departures from the homologous scaling. The increase in the depth of the outer convection zone, where $|N| \simeq 0$, is evident. Also, N increases strongly in the core. This is mainly the result of the increase in the gravitational acceleration (cf. Eq. 2.14) as the star develops a very compact helium core. Thus Model 3 has a helium core with a mass of $0.18 M_{\odot}$, contained within the inner 0.7 % of the stellar radius. In this model the convective envelope is so deep that it extends into a region where the composition has been changed by hydrogen fusion. This causes a discontinuity in the composition and hence the density, giving rise to a spike in the buoyancy frequency, as shown in the figure.

In Fig. 3 are also indicated the dimensionless values $\hat{\omega}_{c,atm}$ of the acoustic cut-off frequency in the atmospheres of the three models. Since this is determined by the atmospheric properties of the star it does not follow the homologous frequency scaling. In fact, using Eq. (2.13) for $\nu_{c,atm} = \omega_{c,atm}/2\pi$ and the scaling in Eq. (2.30) for $\Delta\nu$ it follows that

$$\frac{\nu_{c,atm}}{\Delta\nu} \propto M^{1/2} R^{-1/2} T_{eff}^{-1/2}. \quad (2.31)$$

Since $\nu_{c,atm}$ is an upper limit to the frequencies of modes trapped in the stellar interior, this ratio, according to Eq. (2.19), provides a measure of the number of acoustic modes that are trapped. This obviously decreases as the star evolves up the red-giant branch.

Figure 3 also shows that in Models 2 and 3 the maximum of \hat{N} in the core is substantially higher than $\hat{\omega}_{c,atm}$. This means that *all* trapped nonradial modes satisfy $\omega < N, S_l$ in the core and hence behave like g modes there, while they may behave as acoustic modes in the outer parts of the star where $\omega > N, S_l$. The overall character of the mode then depends on whether it has the largest amplitude in the g-mode or the p-mode region, and hence, effectively, on the behaviour in the intermediate region. If the eigenfunction decreases exponentially with depth in this region the mode has its largest amplitude in the outer region of the star and it may be said to be *p-dominated*. In the opposite case, with an eigenfunction increasing with depth, the amplitude is largest in the core and the mode is *g-dominated*. These two conditions essentially require the frequency to be determined such that the mode resonates with the outer acoustic, and the inner buoyancy-driven, cavity, respectively. For the p-dominated modes this leads to Eq. (2.18) for the frequencies, which may be cast, at least approximately, in the form of Eq. (2.19). For the g-dominated modes we similarly find that the frequencies satisfy Eqs (2.23) or (2.24). For evolved red giants like Model 3, with a very high buoyancy frequency in the core, the period spacing Π_0/L (cf. Eq 2.25) becomes very small and hence the density of the g-dominated modes is much higher than the density of p-dominated modes, whose frequency spacing is given by $\Delta\nu$. It should also be noted that the high density of g-dominated modes correspond to an extremely high number of nodes in the eigenfunctions in the core, requiring substantial care in the numerical computation of the oscillations.

The properties of the modes can be illustrated by considering the normalized mode inertia

$$E = \frac{\int_V \rho |\delta \mathbf{r}|^2 dV}{M |\delta \mathbf{r}|_s^2}, \quad (2.32)$$

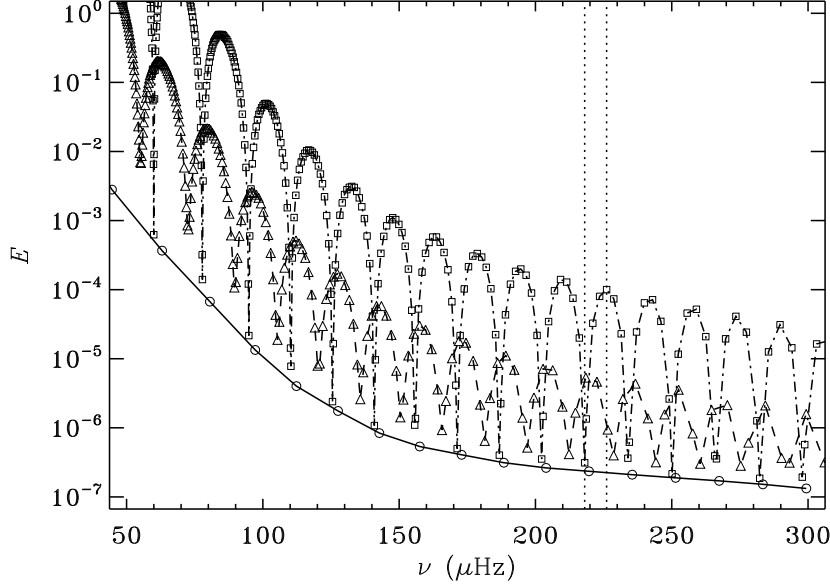


FIGURE 4. Dimensionless inertia (cf. Eq. 2.32) for Model 3 in the $1 M_{\odot}$ evolution sequence illustrated in Fig. 1. Radial modes are shown with circles connected by solid lines, $l = 1$ modes with triangles connected by dashed lines and $l = 2$ modes with squares connected by dot-dashed lines. The vertical dotted lines mark the $l = 2$ modes for which the eigenfunctions are illustrated in Fig. 5.

where the integral is over the volume V of the star and $|\delta \mathbf{r}|_s^2$ is the surface value of the squared norm of the displacement vector $\delta \mathbf{r}$. This is shown in Fig. 4 for modes of degree $l = 0 - 2$ in Model 3. The radial modes ($l = 0$) are purely acoustic, with an inertia that decreases with increasing frequency. For $l = 1$ and 2, on the other hand, there is a dense set of g-dominated modes, with acoustic resonances where the inertia approaches the value for the radial modes at the corresponding frequency. The pattern of these resonances is very similar to Eq. (2.19), with the $l = 1$ resonances roughly half-way between the $l = 0$ frequencies and a small separation between an $l = 2$ resonance and the neighbouring $l = 0$ mode.

Figure 5 shows a few selected eigenfunctions, in the form of scaled radial component of the displacement, normalized to unity at the surface. The comparison between the neighbouring $l = 0$ and 2 modes in panel a) shows that they are very similar in the bulk of the star where the $l = 2$ mode is predominantly of acoustic character. In the core the eigenfunction for $l = 2$ varies rapidly but at generally small amplitude for this p-dominated mode, as seen in panel b). The behaviour in the core for the mode shown in panel c) is very similar, but at a much higher amplitude relative to the surface normalization, and corresponding to the local maximum in the inertia. We discuss the consequences for the observable visibility of the modes in Section 5 below.

3. Damping and excitation of solar-like oscillations

When nonadiabatic effects are taken into account, the oscillation frequencies are no longer real. Assuming again a time dependence as $\exp(-i\omega t)$ and writing $\omega = \omega_r + i\omega_i$ in terms of real and imaginary parts, the real part ω_r determines the frequency of the mode

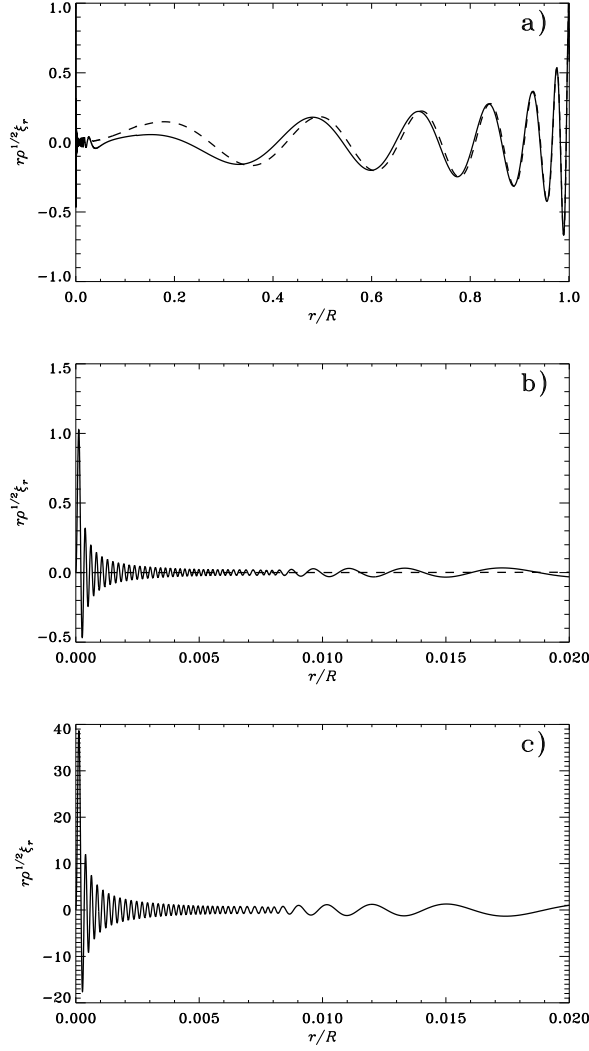


FIGURE 5. Scaled eigenfunctions, normalized at the surface, for Model 3 in the $1 M_{\odot}$ evolution sequence shown in Fig. 1. The quantity shown is $r\rho^{1/2}\xi_r$, where ξ_r is the amplitude of the vertical displacement. In panels a) and b) the dashed line shows a radial mode with cyclic frequency $\nu = 219.6 \mu\text{Hz}$ and mode inertia (cf. Eq. 2.32) $E = 2.35 \times 10^{-7}$, and the solid line shows a p-dominated $l = 2$ mode with $\nu = 218.1 \mu\text{Hz}$ and $E = 3.12 \times 10^{-7}$. In panel c) is illustrated a neighbouring g-dominated $l = 2$ mode with $\nu = 226.1 \mu\text{Hz}$ and $E = 1.00 \times 10^{-4}$.

whereas the imaginary part ω_i determines the growth or decay of the amplitude, $\omega_i < 0$ corresponding to a damped mode. The determination of the damping or excitation of the modes requires a solution of the full nonadiabatic oscillation equations, introducing also the energy equation and equations for the energy generation and transport. The latter is given by the perturbations to the flux $\mathbf{F} = \mathbf{F}_{\text{rad}} + \mathbf{F}_{\text{con}}$ which, as indicated, has both a radiative (\mathbf{F}_{rad}) and convective (\mathbf{F}_{con}) contribution. The radiative part can be dealt with in a relatively straightforward manner, while the treatment of the convective part remains highly uncertain. Furthermore, a significant contribution to the damping may come from the dynamical effects of convection through the perturbation to the Reynolds

stresses, often approximated by a turbulent pressure p_t , which again is uncertain (e.g., Houdek 2010a).

A convenient way to discuss the damping or excitation of the modes is to express the growth rate, approximately in terms of the *work integral* $W = W_g + W_t$, as

$$\omega_i \simeq \frac{W_g}{J} + \frac{W_t}{J}, \quad (3.1)$$

with

$$\begin{aligned} W_g &= \text{Re} \left[\int_V \frac{\delta \rho^*}{\rho} (\Gamma_3 - 1) \delta(\rho \epsilon - \text{div } \mathbf{F}) dV \right], \\ W_t &= -\omega_r \text{Im} \left[\int_V \frac{\delta \rho^*}{\rho} \delta p_t dV \right], \\ J &= 2\omega_r^2 \int_V \rho |\delta \mathbf{r}|^2 dV = 2\omega_r^2 M |\delta \mathbf{r}_s|^2 E. \end{aligned} \quad (3.2)$$

Here δ denotes the Lagrangian perturbation, i.e., the perturbation following the motion, $\Gamma_3 - 1 = (\partial \ln T / \partial \ln \rho)_{\text{ad}}$, and ϵ is the rate of energy generation per unit mass; also the star indicates the complex conjugate.

Equations (3.1) and (3.2) have a simple physical meaning: In the expression for W_g $\delta(\rho \epsilon - \text{div } \mathbf{F})$ gives the perturbation to the heating rate; thus W_g gets a positive contribution, and hence a contribution to the excitation of the mode, where heating and compression, described by $\delta \rho / \rho$, are in phase. Heating at compression is the basis for the operation of any heat engine, and hence modes that are unstable because of this can be said to be driven by the *heat-engine* mechanism.† Depending on the phase relation between compression and δp_t the term in W_t may contribute to the damping or driving of the mode.

As already indicated, the treatment of the convection-pulsation interaction is a major uncertainty in nonadiabatic calculations for stars with significant outer convection zones, where the convective timescales and the pulsation periods are typically similar. Two generalizations of mixing-length theory have seen fairly widespread use. In one, based on an original model by Unno (1967), steady convective eddies are considered, with a balance between buoyancy and turbulent viscous drag. In the second, developed by Gough (1977), convective eddies are continually created and destroyed. The effects of the perturbations associated with the pulsations on these physical models can then be described, leading to expressions for the perturbations to the convective flux and Reynolds stresses. Unno's description has been further developed (see Grigahcène et al. 2005, and references therein), while Gough's description was developed and applied by, e.g., Balmforth (1992) and Houdek et al. (1999). With judicious (but not unreasonable) choices of parameters both formulations can predict the transition to stability at the red edge of the Cepheid instability strip, as well as yield results for solar models that are consistent with the observationally inferred damping rates.‡ Interestingly, the dominant mechanism resulting in damping of the modes differs between the two formulations: in the calculations based on Gough's formulation damping is dominated by the perturbation to the turbulent pressure, while the results based on Unno's formulation show damping

† Since the perturbation to the heating is often determined by the perturbation to the opacity κ this is also known as the κ mechanism.

‡ A different formulation by Xiong et al. (1997), based on equations for the second- and third-order correlations, similarly predicts the red edge but apparently finds that some of the observed solar modes are unstable (Xiong & Deng 2010).

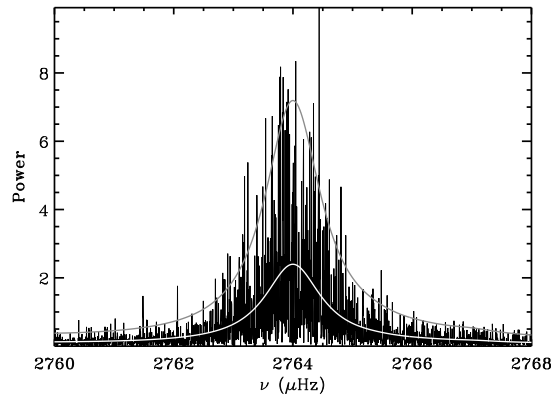


FIGURE 6. Power spectrum of a solar radial mode, from 8 years of BiSON observations. The white curve shows a Lorentzian fit (cf. Eq. 3.3) to the observed spectrum, while the smooth grey curve shows the same fit, but multiplied by a factor three. Data courtesy of W. J. Chaplin; see Chaplin et al. (2002).

through the perturbation to the convective flux. A more detailed comparison of these two sets of results is clearly called for.

The cause of the solar oscillations is now almost universally thought to be stochastic excitation by near-surface convection of the intrinsically stable modes. Stochastic excitation of waves in the solar atmosphere was first considered by Stein (1968), followed by the application to the excitation of normal modes by Goldreich & Keeley (1977). The basic properties of damped oscillations excited by turbulence was considered by Batchelor (1956) (see also Christensen-Dalsgaard et al. 1989). The result is that the power spectrum of a single mode, of natural frequency ω_0 and damping rate ω_i , is

$$P(\omega) \simeq \frac{1}{4\omega_0^2} \frac{P_f(\omega)}{(\omega - \omega_0)^2 + \omega_i^2}, \quad (3.3)$$

where $P_f(\omega)$ is the power spectrum of turbulent forcing. Assuming that P_f varies slowly with frequency the result is a stochastic function modulated by a Lorentzian envelope, with a full width at half maximum of $2|\omega_i|$. An example, from BiSON observations of a solar radial mode, is shown in Fig. 6. From the fitted Lorentzian it is obviously possible to determine the damping rate $|\omega_i|$. Further analyses of the statistical properties of the stochastically excited oscillators were carried out by Kumar et al. (1988) and Chang & Gough (1998). It was shown by Chaplin et al. (1997) that the observed distribution of solar oscillation amplitudes was consistent with the predictions of these analyses.

An early rough prediction of the excitation of solar-like modes in other stars was carried out by Christensen-Dalsgaard & Frandsen (1983). It was shown by Kjeldsen & Bedding (1995) that the resulting velocity amplitudes approximately scaled as L/M , where L is the surface luminosity of the star. Later, more careful investigations (e.g., Houdek et al. 1999; Samadi et al. 2007) confirm that the amplitudes increase with L/M although generally to a power slightly less than one.

The excitation of a specific mode clearly depends on the detailed property of the mode, the amplitude being determined by the balance between the stochastic energy input from convection and the damping. The energy input increases as a high power of the convective velocity (Stein 1968) and hence is dominated by the near-surface layers where convection

is most vigorous. Here the properties of the oscillations depend predominantly on the frequency, with little dependence on the degree (at least for the low-degree modes that are relevant in distant stars). The outcome is that the mean square amplitude can be written as (e.g., Chaplin et al. 2005)

$$\langle A^2 \rangle \simeq \frac{1}{E|\omega_i|} \frac{\mathcal{P}_f(\omega)}{E}, \quad (3.4)$$

where A might be the surface velocity or the relative intensity fluctuation; here $\mathcal{P}_f(\omega)$, which depends on frequency but in general not on degree, describes the energy input from convection (see, e.g., Houdek 2010b, for a review). Also, the damping rate is given by Eqs (3.1) and (3.2). In the common case where the integrals in W_g and W_t are dominated by the near-surface layers it follows that $|\omega_i|E$ is independent of E at constant frequency; consequently, in this case $\langle A^2 \rangle \propto E^{-1}$ at constant frequency. This is important in the discussion of the excitation of solar-like oscillations in red giants where we see large variations in E over a narrow frequency range (cf. Fig. 4): the g-dominated modes, with large inertias, are clearly expected to have a much smaller root-mean-square amplitude than the p-dominated modes with low inertia. However, the question of the mode *visibility*, and hence the likelihood to detect them, is more complicated; we return to this in Section 5.

The balance between energy input and damping leads to a characteristic bell-shaped amplitude distribution of the mean amplitude, although with fluctuations around the mean reflecting the stochastic nature of the excitation. The shape of the amplitude distribution was discussed by Goldreich et al. (1994). They found that the increase in amplitude with frequency at low frequency was predominantly caused by the change in the shape of the eigenfunction as the upper reflection point, where $\omega = \omega_c$ moves closer to the surface with increasing ω . At high frequency this upper reflection point is very close to the photosphere, and the amplitude decreases with increasing frequency due to an increasing mismatch between the oscillation periods and the timescales of the convective eddies that dominate the excitation. As the frequency approaches $\omega_{c,atm}$ beginning energy loss through the stellar atmosphere may also contribute to the damping and hence further decrease the amplitudes. Indeed, the variation with frequency of the damping rate clearly also plays a role for the the variation in amplitude.

It has been found observationally that the cyclic frequency ν_{max} of maximum amplitude appears to scale with the acoustic cut-off frequency $\nu_{c,atm}$ (e.g., Brown et al. 1991; Kjeldsen & Bedding 1995; Bedding & Kjeldsen 2003; Stello et al. 2008) (see also Bedding, this volume), and hence follows the scaling in Eq. (2.13). This scaling has been a very useful tool in characterizing the observed properties of stars showing solar-like oscillations (e.g., Kallinger et al. 2010), but the relation between ν_{max} and $\nu_{c,atm}$ still defies a definite theoretical understanding. Belkacem et al. (2011) noted that the location of ν_{max} is closely related to the plateau in damping rates at intermediate frequency, apparently caused by a resonance between the pulsation period and the local thermal timescale, a feature already noticed by Gough (1980) and Christensen-Dalsgaard et al. (1989). However, this does not fully explain the observed tight relation.

4. Do red giants have nonradial oscillations?

As pointed out by Kjeldsen & Bedding (1995) the amplitude predictions by Christensen-Dalsgaard & Frandsen (1983) scaled as L/M . Thus one could expect to see solar-like oscillations in red giants with quite substantial amplitudes. Early evidence was found for such oscillations in Arcturus (Smith et al. 1987; Innis et al. 1988) while Edmonds & Gilliland (1996) identified

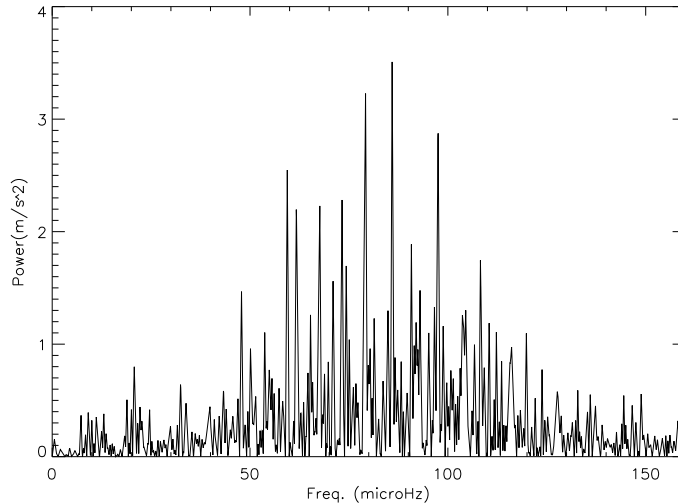


FIGURE 7. Power spectrum of the G7 giant ξ Hydrae, from one month of Doppler velocity measurements. Adapted from Frandsen et al. (2002).

oscillations in K giants in the globular cluster 47 Tuc. Christensen-Dalsgaard et al. (2001) noted that the statistics of very long-period semi-regular variables observed by the American Association of Variable Star Observers appeared to obey amplitude statistics consistent with stochastic excitation, strongly suggesting that the variability of these stars was also solar-like, although at month-long periods and with amplitudes allowing simple visual observations. Photometric observations of the oscillations in Arcturus were carried out by Retter et al. (2003) with the WIRE satellite. Analyses of large samples of red giants observed by OGLE[†] (e.g. Kiss & Bedding 2003, 2004; Soszyński et al. 2007) showed oscillations in several modes, and Dziembowski & Soszyński (2010) confirmed that the most likely cause was solar-like oscillations. In a further analysis of ground-based survey observations of red giants in the Galaxy and the Large Magellanic Cloud Tabur et al. (2010) demonstrated a continuous transition between pulsations in G and K giants and those seen in very luminous M giants.

The first detailed observations of the oscillations of a red giant was carried out by Frandsen et al. (2002) for the G7 giant ξ Hya. The resulting power spectrum is shown in Fig. 7. This clearly shows peaks at uniformly spaced frequency, in accordance with Eq. (2.19), and a power envelope very similar to what is observed in the Sun, strongly supporting the solar-like nature of the oscillations. From analysis of the spectrum the separation between the peaks was determined to be $\simeq 7 \mu\text{Hz}$.

Modelling of ξ Hya to match the well determined luminosity and effective temperature is shown in Fig. 8. Stars ascend the red-giant branch while burning hydrogen in a shell around an inert and almost isothermal helium core. As the mass of the core increases, so does the luminosity and the temperature of the core. At the tip of the red-giant branch the temperature reaches a sufficiently high value, around 10^8 K , where helium fusion becomes significant. The resulting change in structure, with an expansion of the core, leads to a reduction in the surface radius and luminosity, with the star entering a phase of stable helium burning. Even during this phase, however, a substantial part of the total energy production takes place in the hydrogen-burning shell. As the phase is relatively

[†] Optical Gravitational Lensing Experiment

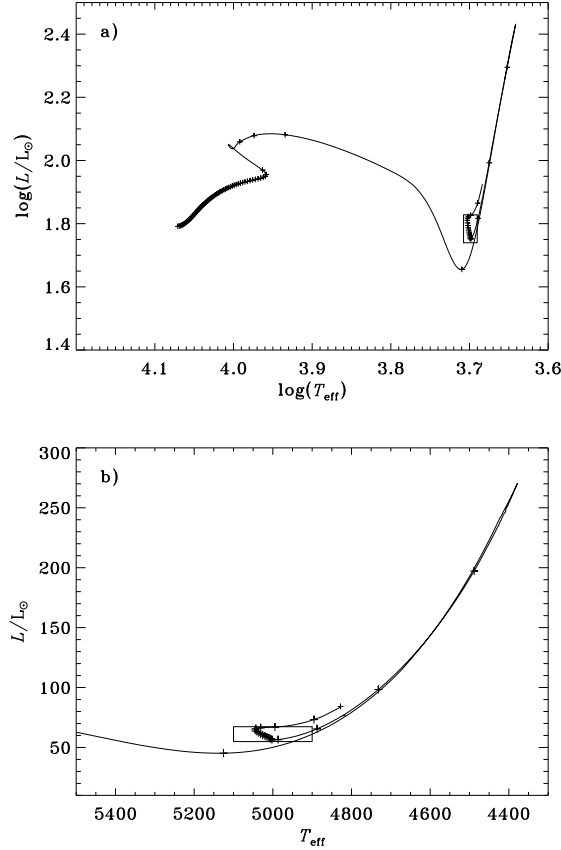


FIGURE 8. Evolution track for a model of ξ Hydrae, with mass $M = 2.8M_\odot$ and heavy-element abundance $Z = 0.019$. The plusses are placed at 5 Myr intervals along the track. The box marks the $1-\sigma$ error box for the observed effective temperature and luminosity.

extended, with a duration of around 20 per cent of that of the central hydrogen-burning main sequence, the chances of observing a star in this phase are fairly high; in stellar clusters such stars populate the so-called ‘red clump’.

As noted by Teixeira et al. (2003) ξ Hya could be identified as being in the ascending phase on the red giant branch. However, since this phase is extremely brief a more likely identification would be with the core helium burning phase. In either case, a match to the observed frequencies was possible only if the observed frequency spacing was identified with $\Delta\nu$, such that only modes of one degree, presumably radial modes, were observed. In contrast, from a strict application of Eq. (2.19) one would have expected the spacing to be $\Delta\nu/2$, and hence $\Delta\nu \simeq 14 \mu\text{Hz}$. However, given the scaling in Eq. (2.30) this would be entirely inconsistent with the location of the star in the HR diagram.

To account for this identification Christensen-Dalsgaard (2004) considered the possibility that all nonradial modes in red giants would likely be heavily damped and hence have small amplitudes. He noted that W_g (cf. Eq. 3.2) depends on $\delta(\text{div } \mathbf{F})$, i.e., on the derivative of $\delta\mathbf{F}$. In turn, roughly $\delta\mathbf{F} \propto \nabla(\delta T)$ and $\delta T/T \propto \delta\rho/\rho \propto \text{div } \delta\mathbf{r}$. It follows that W_g depends on the third derivative of $\delta\mathbf{r}$. Thus even if the amplitude of $\delta\mathbf{r}$ in the core is quite small, as is the case for p-dominated modes (cf. Fig. 5), $\delta(\text{div } \mathbf{F})$ could be quite large for a mode varying very rapidly as a function of r , leading to a substantial

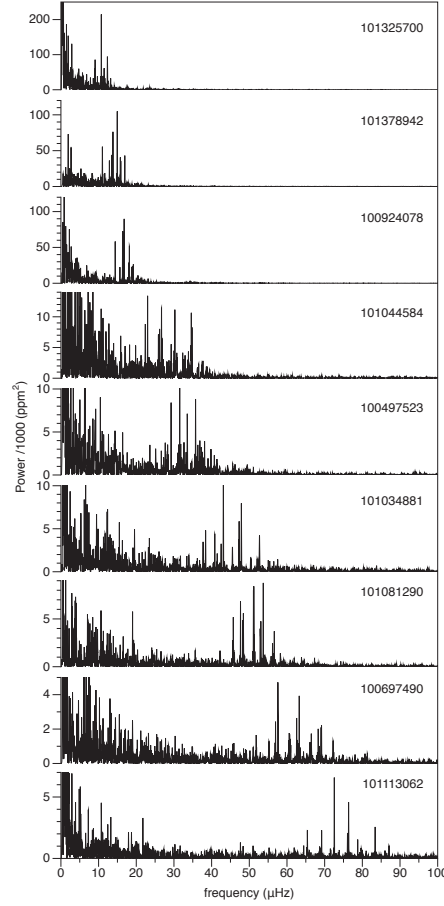


FIGURE 9. Power spectra of solar-like oscillations in red giants, from 5 months of observations with the CoRoT satellite. The panels are labelled by the CoRoT identification number. Radius and luminosity increase towards the top. Figure courtesy of J. De Ridder; from De Ridder et al. (2009).

contribution to the damping from the core for all nonradial modes. Although the analysis was entirely qualitative, Christensen-Dalsgaard (2004) found some support for this conjecture in the analyses by Dziembowski (1977) and Dziembowski et al. (2001).

This pessimistic expectation for red-giant seismology has been completely overturned by observations and an improved theoretical understanding. Hekker et al. (2006) found evidence for nonradial pulsation in the line-profile variation of a few red giants showing solar-like oscillations. Even more dramatically, De Ridder et al. (2009) clearly demonstrated the presence of nonradial solar-like oscillations in a large number of red giants from early CoRoT observations. Figure 9 shows resulting power spectra. The power enhancement from the solar-like oscillations is evident; as stars on the red-giant branch have roughly the same effective temperature, the frequency at maximum power decreases with increasing radius and luminosity in accordance with Eq. (2.13). The observed frequencies satisfy a relation similar to Eq. (2.19), with definite evidence for nonradial modes. This is most clearly illustrated in an *échelle diagram* (see Bedding, this volume), where the frequencies are shown against the frequency reduced modulo $\Delta\nu$, effectively dividing the spectrum into segments of length $\Delta\nu$ and stacking the segments. This has been done for

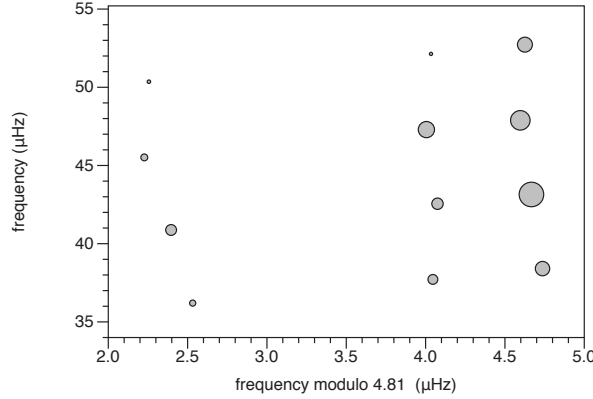


FIGURE 10. Échelle diagram of the star 101034881 in Fig. 9. This corresponds to stacking slices of the power spectrum of a length given the large separation $\Delta\nu = 4.81 \mu\text{Hz}$: the abscissa is the frequency modulo $\Delta\nu$ whereas the ordinate is the frequency. Figure courtesy of J. De Ridder; from De Ridder et al. (2009).

one of the stars in Fig. 10. In accordance with Eq. (2.19) the three columns of points correspond to modes of degree $l = 0$ and 2 to the right, separated by the small separation, and modes with $l = 1$ to the left. Analyses of red giants observed by CoRoT and *Kepler* (e.g., Huber et al. 2010; Mosser et al. 2011a) have shown that this frequency pattern is universal amongst red giants.

The very long time series obtained by CoRoT and in particular *Kepler* have allowed fits to the power spectra in terms of the Lorentzian profiles (cf. Eq. 3.3) and hence a determination of the mode damping rates or, equivalently, the lifetimes $\tau = 1/|\omega_i|$. For red giants this yields lifetimes near the maximum amplitude of around 15 days (Huber et al. 2010; Baudin et al. 2011). Interestingly, this is very similar to the value obtained for ξ Hya by Houdek & Gough (2002), using a convection treatment based on Gough (1977).

5. Amplitudes of solar-like oscillations in red giants

To interpret the observations a more detailed analysis of the mode excitation and visibility is required. The analysis leading to Eq. (3.4) determines the mean square amplitude of the mode, corresponding essentially to the area under the corresponding peak in the power spectrum. However, it was noted by Chaplin et al. (2005) that ability to detect a mode in the power spectrum depends instead on the *peak height* H , related to A^2 † by

$$A^2 = |\omega_i| H, \quad (5.1)$$

since $|\omega_i|$ determines the width of the peak. If the damping is dominated by the near-surface layers, it was argued above that both A^2 and $|\omega_i|$ are proportional to E^{-1} at a given frequency. It then follows from Eq. (5.1) that H is independent of E , i.e., that all modes in a given frequency interval are excited to roughly the same amplitude. For the dense spectrum of modes in a red giant, such as illustrated in Fig. 4, the result would be a very dense observed power spectrum, with no indication of the acoustic resonances approximately satisfying Eq. (2.19). This is in obvious contradiction to, e.g., the observations by De Ridder et al. (2009).

This argument, however, neglects the fact that the oscillations are observed for a finite

† for simplicity, we drop $\langle \dots \rangle$ in the following

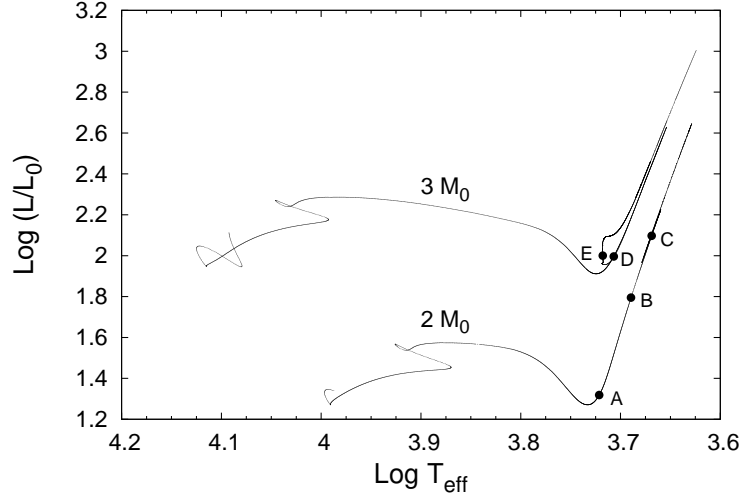


FIGURE 11. Evolution tracks for models of mass 2 and $3 M_{\odot}$, for which Dupret et al. (2009) considered the stochastic excitation of solar-like oscillations. Figure courtesy of M.-A. Dupret.

time \mathcal{T} which, for the g-dominated modes, is typically shorter than the lifetime τ of the mode. The resulting peaks in the power-density spectrum has a width that, for $\mathcal{T} \ll \tau$, is proportional to \mathcal{T}^{-1} and hence a correspondingly smaller peak height, very likely making the modes invisible. As a convenient interpolation between the two extremes, Fletcher et al. (2006) proposed the relation

$$H \propto \frac{A^2}{|\omega_i| + 2/\mathcal{T}}. \quad (5.2)$$

A detailed and very illuminating analysis of the excitation of modes in red giants was carried out by Dupret et al. (2009). They considered several red-giant models, with locations in the HR diagram as illustrated in Fig. 11, carrying out nonadiabatic calculations of nonradial modes using the convection formalism of Grigahcène et al. (2005). From a model of the stochastic energy input (e.g., Belkacem et al. 2006) they then computed the expected amplitudes of the modes and the resulting power-density diagrams. They assumed an observing period \mathcal{T} of 150 days, corresponding to CoRoT long runs. Rather than using Eq. (5.2) they effectively adopted $H \propto \tau A^2$ for $\tau > \mathcal{T}/2$ and $H \propto \mathcal{T} A^2/2$ otherwise, with a continuous transition between the two cases. Here we briefly consider their results for Models A and B.

Figure 12 shows the mode lifetimes for modes of degree $l = 0 - 2$ in Model A. In this case the damping is dominated by the near-surface layers and hence, as is obvious in the figure, the variation of τ reflects the behaviour of E which is qualitatively similar to the case illustrated in Fig. 4. For $l = 2$ the g-dominated modes have lifetimes substantially higher than the assumed $\mathcal{T}/2$, indicated in the figure by a horizontal dashed line. On the other hand, the $l = 1$ modes at higher frequency all have lifetimes at or below the observing time, and hence would be expected to reach similar peak heights in a given frequency interval. This is confirmed by Fig. 13 which shows the predicted peak heights. The overall envelope seems to be somewhat skewed towards lower frequency, relative to what is expected from the observed scaling with the acoustic cut-off frequency; given the uncertainties in modelling both the damping and the energy input, this is hardly surprising. However, it is striking that while the $l = 2$ modes show strong acoustic

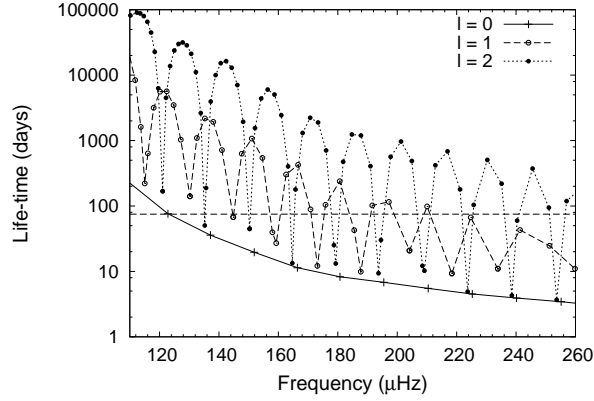


FIGURE 12. Computed lifetimes of Model A in Fig. 11, at the base of the $2M_{\odot}$ red-giant branch. Modes of degree $l = 0, 1$ and 2 are shown, respectively, by plusses connected by solid lines, open circles connected by dashed lines and closed circles connected by dotted lines. The horizontal dashed line marks a damping time of 75 d, corresponding to the border between unresolved and resolved modes for a CoRoT long run of 150 days. Figure courtesy of M.-A. Dupret; from Dupret et al. (2009).

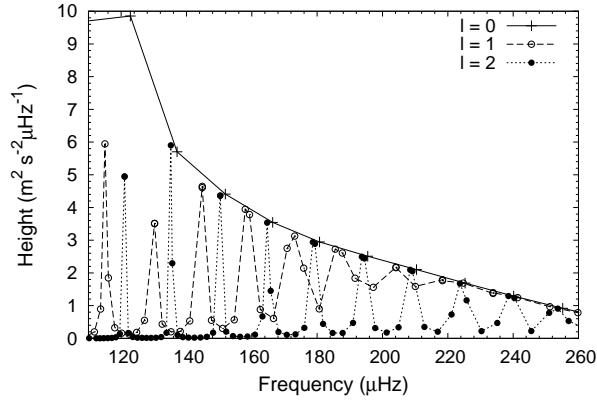


FIGURE 13. Estimated peak heights in the power spectrum of solar-like oscillations in Model A in Fig. 11, at the base of the red-giant branch; for symbol and line styles, see caption to Fig. 12. Figure courtesy of M.-A. Dupret; from Dupret et al. (2009).

resonances, with small peak heights for the g-dominated modes, the $l = 1$ modes at high frequency all reach peak heights comparable with those for the radial modes. It is obvious that such a spectrum can be quite complex (see also Di Mauro et al. 2011).

The situation is rather different for the more evolved Model B. As illustrated in Fig. 14 there is now strong damping in the core for the g-dominated modes with $l = 2$; for $l = 1$ the same is the case at relatively low frequency, while the surface layers dominate at high frequency. The damping in the core is a result of the very rapidly oscillating eigenfunctions in the core, as discussed above. Owing to the increased central condensation the buoyancy frequency is substantially higher than in Model A, leading to a higher vertical wave number and hence stronger damping in the core. For p-dominated modes, on the other hand, the damping is still dominated by the near-surface layers. Together with a strong trapping of the g-dominated modes in the core, this leads to a much stronger contrast

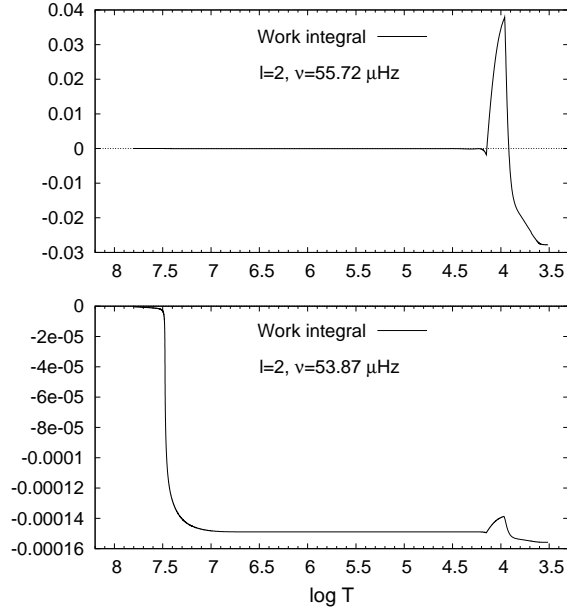


FIGURE 14. Work integrals for the intermediate red-giant branch $2 M_{\odot}$ Model B in Fig. 11; this essentially corresponds to the partial integrals of $W_g + W_t$, defined in Eq. (3.2), and here plotted against temperature T in the model. The top panel is for a p-dominated mode while the bottom panel is for a g-dominated mode largely trapped in the core. Figure courtesy of M.-A. Dupret; from Dupret et al. (2009).

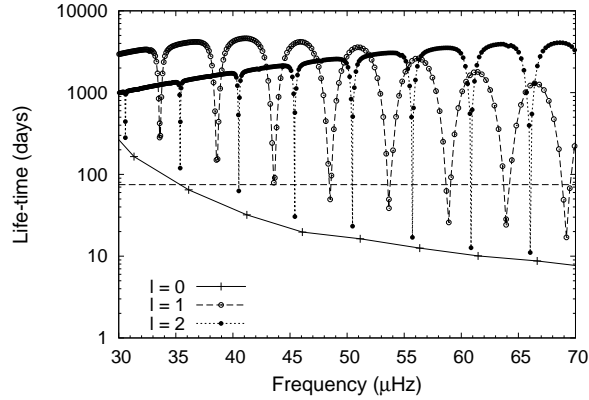


FIGURE 15. Computed lifetimes for the intermediate red-giant branch $2 M_{\odot}$ Model B in Fig. 11; see caption to Fig. 12. Figure courtesy of M.-A. Dupret; from Dupret et al. (2009).

in lifetime between the p- and g-dominated modes, with the latter having lifetimes very substantially higher than the observing time (cf. Fig. 15). The effect of this on the predicted power density spectrum is evident in Fig. 16: there are now obvious acoustic resonances for both $l = 1$ and 2. The $l = 2$ resonances are confined to very narrow frequency intervals, caused also by the more extended evanescent region between the peak in the buoyancy frequency and the region of acoustic propagation, and typically involve only 1 – 2 modes at non-negligible peak heights. For $l = 1$, on the other hand,

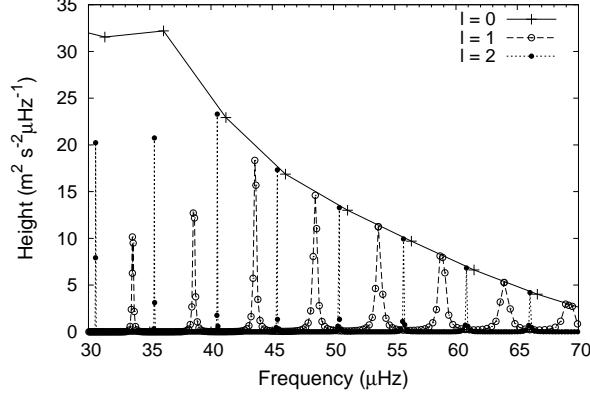


FIGURE 16. Estimated peak heights in the power spectrum of solar-like oscillations in the intermediate red-giant branch $2 M_{\odot}$ Model B in Fig. 11; for symbol and line styles, see caption to Fig. 12. Figure courtesy of M.-A. Dupret; from Dupret et al. (2009).

there is typically a cluster of peaks with heights that may make the modes observable. As discussed by Bedding (this volume) this was found to be the case by Beck et al. (2011) and Bedding et al. (2011). We discuss the significance of these results in the following section.

6. Asteroseismic diagnostics in red giants

Detection of solar-like oscillations in red giants, such as illustrated in Fig. 9, almost immediately provides a measure of the large frequency separation $\Delta\nu$ and the frequency ν_{\max} of maximum power. These basic quantities already have a substantial diagnostic potential: $\Delta\nu$ approximately satisfies the scaling (Eq. 2.30) with the mean density and it can be assumed that ν_{\max} scales as the atmospheric acoustic cut-off frequency (Eq. 2.13). If T_{eff} is known from photometric or spectroscopic observations one can then determine the radius and mass of the star as

$$\frac{R}{R_{\odot}} = \frac{\nu_{\max}}{\nu_{\max,\odot}} \left(\frac{\Delta\nu}{\Delta\nu_{\odot}} \right)^{-2} \left(\frac{T_{\text{eff}}}{T_{\text{eff},\odot}} \right)^{1/2} \quad (6.1)$$

and

$$\frac{M}{M_{\odot}} = \left(\frac{R}{R_{\odot}} \right)^3 \left(\frac{\Delta\nu}{\Delta\nu_{\odot}} \right)^2, \quad (6.2)$$

where \odot denotes solar values (e.g., Kallinger et al. 2010). Such analyses provide unique possibilities for population studies of field red giants (e.g., Miglio et al. 2009; Mosser et al. 2010; Hekker et al. 2011). Stellar modelling provides further constraints on the relation between T_{eff} , M and R and hence a more precise determination of stellar properties (Gai et al. 2011), as used in an analysis of red giants in two of the open clusters in the *Kepler* field by Basu et al. (2011).

As discussed in connection with Eq. (2.21), for main-sequence stars the small frequency separations $\delta\nu_{l+2}(n) = \nu_{nl} - \nu_{n-1,l+2}$ provide a measure of the age of the star. This no longer holds for red giants. Here in most cases $\delta\nu_{l+2}$ scales essentially as the large frequency separation and hence mainly reflects the variation of the mean density of the star (e.g., Bedding et al. 2010; Huber et al. 2010; Mosser et al. 2011a). This is a natural consequence of the fact that the propagation region of the nonradial acoustic modes for such

[thp]

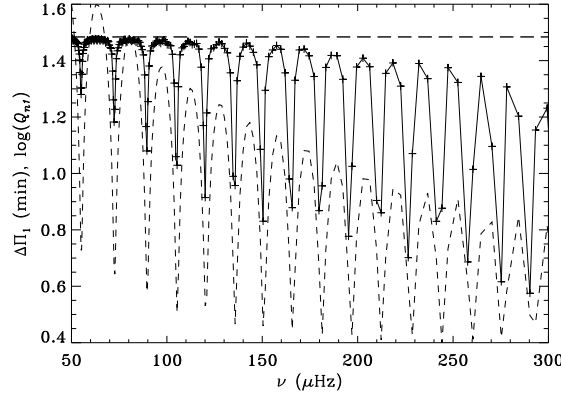


FIGURE 17. The solid curve shows the period spacing between adjacent $l = 1$ modes in Model 3 in the $1M_{\odot}$ sequence in Fig. 1. The horizontal dashed line shows the asymptotic value for pure g modes, from Eq. (6.4). For comparison, the short-dashed curve shows the logarithm of the normalized inertia Q_{nl} (cf. Eq. 6.3) on an arbitrary scale.

stars lies in the convective envelope, which probably changes in a largely homologous fashion as the properties of the star change. A detailed analysis of the diagnostic potential of acoustic modes in red giants was carried out by Montalbán et al. (2010). They also considered other types of small frequency separations, such as $\delta\nu_{01}(n) = (\nu_{n0} + \nu_{n+10})/2 - \nu_{n1}$. Interestingly, they found that for models with somewhat shallower convective envelopes, particularly amongst core helium-burning stars, where the lower turning point of the $l = 1$ modes was in the radiative region, the average $\langle\delta\nu_{01}\rangle/\Delta\nu$ showed a marked dependence on the distance from the base of the convective envelope to the turning point.

The asymptotic analysis leading to Eq. (2.19) for the acoustic-mode frequencies assumes that the equilibrium structure varies slowly compared with the eigenfunctions. There are regions in the star where this does not hold, with variations in the sound speed on a scale that is comparable with or smaller than the local wavelength. This causes periodic variations in the frequencies with properties that depend on the depth and nature of the sound-speed feature. In red giants the most important example of such an *acoustic glitch* is related to the second ionization of helium which causes a dip in Γ_1 and hence (cf. Eq. 2.2) a localized variation in the sound speed. This variation provides a diagnostics of the helium abundance in the star (e.g., Gough 1990; Vorontsov et al. 1991; Basu et al. 2004; Monteiro & Thompson 2005; Houdek & Gough 2007). A clear signature of this effect was found by Miglio et al. (2010) in a red giant observed by CoRoT. They noted, following an earlier discussion by Mazumdar (2005) of the diagnostic potential of such glitches, that the inferred depth of the sound-speed feature together with large frequency separation provide a purely asteroseismic determination of the mass and radius of the star. This feature can probably be detected in a substantial fraction of the red giants observed with CoRoT and *Kepler*, promising a determination of the so far poorly known helium abundance in these stars and hence important constraints on the chemical evolution of the Galaxy.

From the analysis by Dupret et al. (2009), discussed in Section 5, we noted that for $l = 1$ several modes might be excited to observable amplitudes in the vicinity of an acoustic resonance. This is consistent with the rather larger scatter for these dipolar modes observed by Bedding et al. (2010) in an collapsed échelle diagram based on early *Kepler*

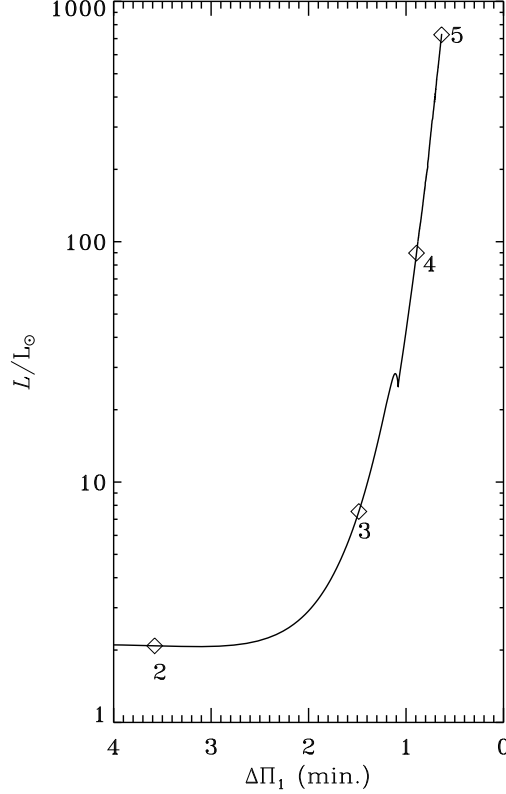


FIGURE 18. ‘Hertzsprung-Russell diagram’, in terms of the asymptotic dipolar g-mode spacing $\Delta\Pi_1$ (cf. Eq. 6.4) and luminosity, for the $1 M_\odot$ evolution track illustrated in Fig. 1.

data and, as noted by Montalbán et al. (2010), has important diagnostic potential. As discussed by Bedding (this volume) this potential was dramatically realized in the analyses by Beck et al. (2011) and Bedding et al. (2011). The groups of dipolar peaks near the acoustic resonances were found to have a regular structure which allowed determination of well-defined period spacings, reminiscent of the behaviour of g modes (cf. Eq. 2.24) and matching a corresponding behaviour in the computed frequencies of stellar models. Such behaviour has also been found in analysis of CoRoT data (Mosser et al. 2011b).

To illustrate the properties of the computed period spacings Fig. 17 shows the difference in period between adjacent dipolar modes in Model 3 in the $1 M_\odot$ evolution sequence illustrated in Fig. 1. It is clear that, particularly in the dense region of g-dominated modes at relatively low frequency, there is an almost uniform spacing, interspersed with decreases which are associated with the acoustic resonances. To illustrate this relation, the figure also shows $\log Q_{nl}$ where Q_{nl} is the mode inertia normalized by the inertia of a radial mode at the same frequency. Specifically,

$$Q_{nl} = \frac{E_{nl}}{\bar{E}_0(\omega_{nl})}, \quad (6.3)$$

where E_{nl} is the inertia of the mode and $\bar{E}_0(\omega_{nl})$ is the inertia of radial modes, interpolated to the frequency ω_{nl} of the mode. It is obvious that the variation in the period spacing is closely related to the variation in the inertia.

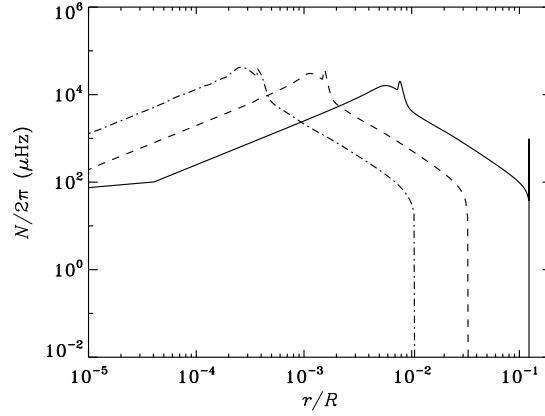


FIGURE 19. Cyclic buoyancy frequencies $N/2\pi$ in Model 3 (solid), Model 4 (dashed) and Model 5 (dot-dashed) in the $1 M_{\odot}$ evolution sequence illustrated in Figs 1 and 18.

The uniform period spacing is clearly only realized for the most g-dominated modes whose high inertia makes detection unlikely.[†] However, it was demonstrated by Bedding et al. (2011) that with the *Kepler* data the pure g-mode period spacing can be determined from the observed frequencies in data of sufficient quality; this was illustrated in a ‘g-mode échelle diagram’, dividing the spectrum into segments of fixed length in period (see also Bedding, this volume). In other cases the period spacings can be inferred from analysis of the power spectra and extrapolated to the value for pure g modes (see also Mosser et al. 2011b). Bedding et al. (2011) showed that the inferred period spacing is substantially higher for clump stars in the core helium burning phase than for stars on the ascending red-giant branch, providing a clear separation into these two groups of stars that are superficially very similar.

From the asymptotic results in Eqs (2.24) and (2.25) the period spacing for pure dipolar g modes is approximately given by

$$\Delta\Pi_1 = \sqrt{2}\pi^2 \left(\int_{r_1}^{r_2} N \frac{dr}{r} \right)^{-1}. \quad (6.4)$$

This is illustrated by the dashed horizontal line in Fig. 17; it is clearly in good agreement with the value obtained from the most strongly trapped modes. Given the $\Delta\Pi_1$, as discussed above, can be obtained from the observations, we therefore obtain diagnostics of the buoyancy frequency in the core of the star.

This can be used to illustrate the evolution of the star in an ‘HR’ diagram, plotting L against $\Delta\Pi_1$, as done in Fig. 18. It is evident that $\Delta\Pi_1$ varies little as the star moves up the red-giant branch. This behaviour can be understood in terms of the variation in the buoyancy frequency, illustrated for three representative models in Fig. 19. On this logarithmic r scale the main effect is a shift towards smaller radii as the core contracts, with little change in the shape of N . Noting that the integral in Eq. (6.4) is in terms of $\log r$ it follows that there is little change in $\Delta\Pi_1$ with evolution. It should also be noticed that N is depressed in the core of the star. This is probably caused by the increasing electron degeneracy of the gas, leading to $d \ln p / d \ln \rho$ approaching $5/3$.[‡]

[†] except perhaps in extremely long timeseries, exceeding the lifetimes of even these modes

[‡] In white dwarfs this leads to a very small buoyancy frequency in the interior of the star, confining the g modes to the outer layers (Fontaine & Brassard 2008).

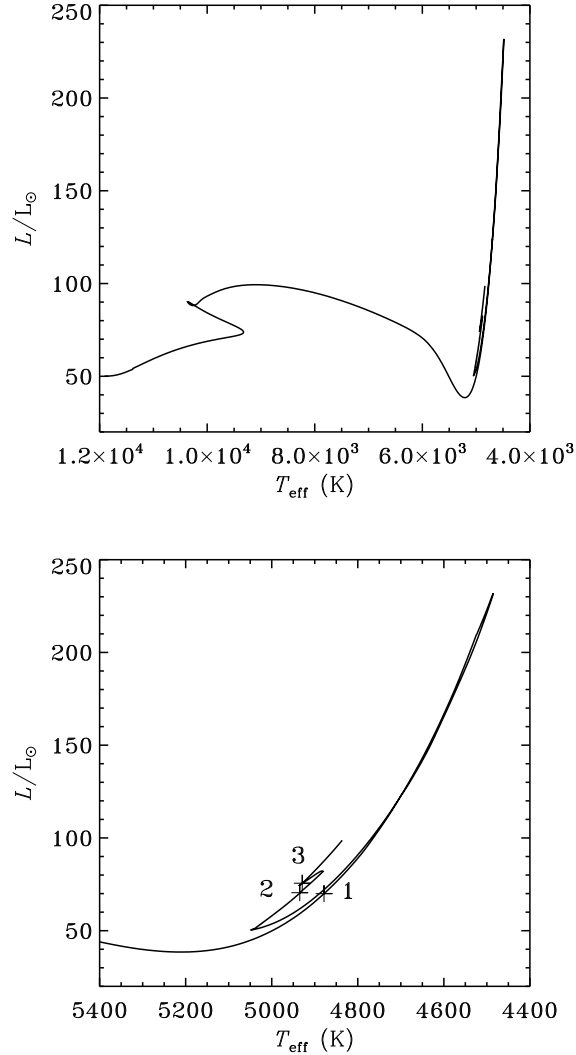


FIGURE 20. Evolution track for a $2.5 M_{\odot}$ model. The track goes through helium ignition at the tip of the red-giant branch and ends near central helium exhaustion.

As discussed by Bedding (this volume) there is a striking difference in $\Delta\Pi_1$ between stars in the hydrogen shell-burning phase, as the $1 M_{\odot}$ model illustrated above, and models that burn helium in the core. Unfortunately ASTEC does not allow computation of a model through a helium flash, and hence the evolution of the $1 M_{\odot}$ model cannot be followed beyond helium ignition. For more massive stars the helium ignition takes place in a more quiet manner which can be followed by ASTEC. Figure 20 shows the evolution track of a $2.5 M_{\odot}$ model up to a point near exhaustion of helium at the centre.

In the $(\Delta\Pi_1, L)$ diagram this leads to a rather more complex evolution, illustrated in Fig. 21. The variation on the ascending red-giant branch is very similar to the $1 M_{\odot}$ evolution illustrated in Fig. 18. With the helium ignition, the star moves through a somewhat convoluted path, shown dotted in the figure, towards larger $\Delta\Pi_1$, before the

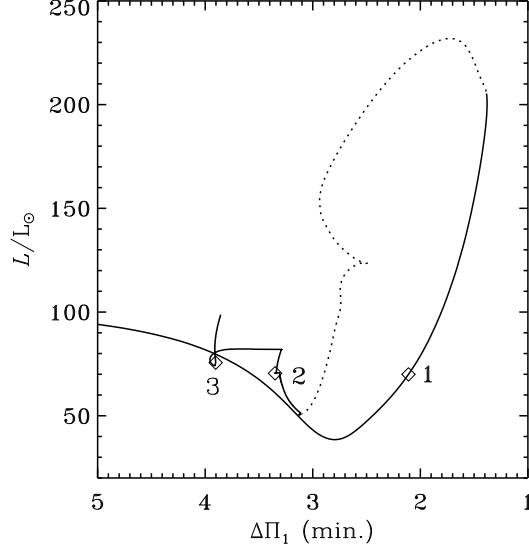


FIGURE 21. ‘Hertzsprung-Russell diagram’, in terms of the asymptotic dipolar g-mode spacing $\Delta\Pi_1$ (cf. Eq. 6.4) and luminosity, for the $2.5 M_\odot$ evolution track illustrated in Fig. 20. The dotted part of the curve extends from helium ignition, at a model age of 0.421 Gyr, to the establishment of stable helium burning, at 0.439 Gyr. (The end of the track is at 0.565 Gyr.)

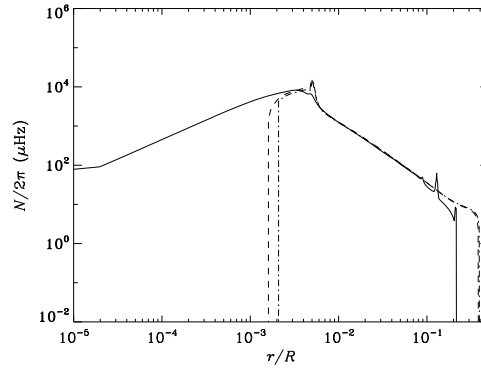


FIGURE 22. Cyclic buoyancy frequencies $N/2\pi$ in Model 1 (solid), Model 2 (dashed) and Model 3 (dot-dashed) in the $2.5 M_\odot$ evolution sequence illustrated in Figs 20 and 21.

star settles down to quiet helium burning.[†] During the central helium burning $\Delta\Pi_1$ undergoes a further jump to smaller larger values, which is also reflected in the evolution track in Fig. 20.

Again, the variation in $\Delta\Pi_1$ can be understood by considering the evolution of the buoyancy frequency, illustrated in Fig. 22. Comparing Models 1 and 2, at roughly the same luminosity, the former model is obviously similar to the red-giant $1M_\odot$ model in Fig. 19. In Model 2, on the other hand, helium burning causes a convective core where

[†] The additional variations along this path appear to be related to modest oscillations in the central properties, similar to, but of smaller amplitude, than the oscillations seen in a full-fledged helium flash (Serenelli & Weiss 2005).

the g modes are excluded; since the behaviour of N in the rest of the core is quite similar to that of Model 1, the effect is to decrease the integral in Eq. (6.4) and hence to increase $\Delta\Pi_1$. This is the dominant cause of the remarkable difference in the period spacing between stars on the red-giant branch and in the red clump observed by Bedding et al. (2011) and discussed further by Bedding in this volume. The subsequent jump in $\Delta\Pi_1$ and L is caused by a jump in the size of the convective core, as illustrated in Fig. 22 by Model 3, probably associated with changes in the composition profile in the core (e.g., Castellani et al. 1971).

This analysis provides a simple explanation for the behaviour found by Bedding et al. (2011) and furthermore indicates how this may allow the period spacing to be used as a sensitive diagnostics of the buoyancy frequency in the stellar core. Further investigations will be required to obtain a deeper understanding of the diagnostic power of such data, including the ability to probe effects of convective overshoot and rotationally induced mixing in the core.

I am very grateful to Pere Pallé and his colleagues at the IAC for the organization of an excellent Winter School. I look forward to the next opportunity to participate in such a school. J. De Ridder and M.-A. Dupret are thanked for providing several key figures.

REFERENCES

- Aerts, C., Christensen-Dalsgaard, J. & Kurtz, D. W. 2010, *Asteroseismology*, Springer, Heidelberg
- Angulo, C., Arnould, M., Rayet, M., Descouvemont, P., Baye, D., et al. 1999, *Nucl. Phys. A*, 656, 3
- Baglin, A., Auvergne, M., Barge, P., Deleuil, M., Michel, E. and the CoRoT Exoplanet Science Team 2009, in *Proc. IAU Symp. 253, Transiting Planets*, eds F. Pont, D. Sasselov & M. Holman, IAU and Cambridge University Press, p. 71
- Balmforth, N. J. 1992, *MNRAS*, 255, 603
- Barban, C., Matthews, J. M., De Ridder, J., Baudin, F., Kuschnig, R., et al. 2007, *A&A*, 468, 1033
- Basu, S., Mazumdar, A., Antia, H. M. & Demarque, P. 2004, *MNRAS*, 350, 277
- Basu, S., Grundahl, F., Stello, D., Kallinger, T., Hekker, S., et al. 2011, *ApJ*, 729, L10
- Batalha, N. M., Borucki, W. J., Bryson, S. T., Buchhave, L. A., Caldwell, D. A., et al. 2011, *ApJ*, 729, 27
- Batchelor, G. K. 1956, *The theory of homogeneous turbulence*. Cambridge University Press
- Baudin, F., Barban, C., Belkacem, K., Hekker, S., Morel, T., et al. 2011, *A&A*, 529, A84
- Beck, P. G., Bedding, T. R., Mosser, B., Stello, D., Garcia, R. A., et al. 2011, *Science*, 332, 205.
- Bedding, T. R. & Kjeldsen, H. 2003, *PASA*, 20, 203
- Bedding, T. R., Huber, D., Stello, D., Elsworth, Y. P., Hekker, S., et al. 2010, *ApJ*, 713, L176
- Bedding, T. R., Mosser, B., Huber, D., Montalbán, J., Beck, P., et al. 2011, *Nature*, 471, 608
- Belkacem, K., Samadi, R., Goupil, M. J., Kupka, F. & Baudin, F. 2006, *A&A*, 460, 183
- Belkacem, K., Goupil, M. J., Dupret, M. A., Samadi, R., Baudin, F., Noels, A. & Mosser, B. 2011, *A&A*, 530, A142
- Böhm-Vitense, E. 1958, *Z. Astrophys.*, 46, 108
- Borucki, W., Koch, D., Batalha, N., Caldwell, D., Christensen-Dalsgaard, J., Cochran, W. D., Dunham, E., Gautier, T. N., Geary, J., Gilliland, R., Jenkins, J., Kjeldsen, H., Lissauer, J. J. & Rowe, J. 2009, in *Proc. IAU Symp. 253, Transiting Planets*, eds F. Pont, D. Sasselov & M. Holman, IAU and Cambridge University Press, p. 289
- Brown, T. M., Gilliland, R. L., Noyes, R. W. & Ramsey, L. W. 1991, *ApJ*, 368, 599
- Castellani, V., Giannone, P. & Renzini, A. 1971, *Ap&SS*, 10, 340
- Chang, H.-Y. & Gough, D. O. 1998, *Solar Phys.*, 181, 251
- Chaplin, W. J., Elsworth, Y., Howe, R., Isaak, G. R., McLeod, C. P., Miller, B. A. & New, R. 1997, *MNRAS*, 287, 51

- Chaplin, W. J., Elsworth, Y., Isaak, G. R., Marchenkov, K. I., Miller, B. A., New, R., Pinter, B. & Appourchaux, T. 2002, *MNRAS*, 336, 979
- Chaplin, W. J., Houdek, G., Elsworth, Y., Gough, D. O., Isaak, G. R. & New, R. 2005, *MNRAS*, 360, 859
- Chaplin, W. J., Kjeldsen, H., Christensen-Dalsgaard, J., Basu, S., Miglio, A., et al. 2011, *Science*, 332, 213
- Christensen-Dalsgaard, J. 2004, *Solar Phys.*, 220, 137
- Christensen-Dalsgaard, J. 2008a, *Ap&SS*, 316, 13
- Christensen-Dalsgaard, J. 2008b, *Ap&SS*, 316, 113
- Christensen-Dalsgaard, J. & Frandsen, S. 1983, *Solar Phys.*, 82, 469
- Christensen-Dalsgaard, J. & Thompson, M. J. 2011, in *Proc. IAU Symposium 271: Astrophysical dynamics: from stars to planets*, eds N. Brummell, A. S. Brun, M. S. Miesch & Y. Ponty, IAU and Cambridge University Press, in the press [[arXiv:1104.5191](#)]
- Christensen-Dalsgaard, J., Gough, D. O. & Libbrecht, K. G. 1989, *ApJ*, 341, L103
- Christensen-Dalsgaard, J., Kjeldsen, H. & Mattei, J. A. 2001, *ApJ*, 562, L141
- Christensen-Dalsgaard, J., Kjeldsen, H., Brown, T. M., Gilliland, R. L., Arentoft, T., Frandsen, S., Quirion, P.-O., Borucki, W. J., Koch, D. & Jenkins, J. M. 2010, *ApJ*, 713, L164
- De Ridder, J., Barban, C., Carrier, F., Mazumdar, A., Eggenberger, P., Aerts, C., Deruyter, S. & Vanautgaerden, J. 2006, *A&A*, 448, 689
- De Ridder, J., Barban, C., Baudin, F., Carrier, F., Hatzes, A. P., et al. 2009, *Nature*, 459, 398
- Deubner, F.-L. & Gough, D. O. 1984, *ARAA*, 22, 593
- Di Mauro, M. P., Cardini, D., Catanzaro, G., Ventura, R., Barban, C., et al. 2011, *MNRAS*, in the press [[arXiv:1105.1076](#)]
- Dupret, M.-A., Belkacem, K., Samadi, R., Montalbán, J., Moreira, O., Miglio, A., Godart, M., Ventura, P., Ludwig, H.-G., Grigahcène, A., Goupil, M.-J., Noels, A. & Caffau, E. 2009, *A&A*, 506, 57
- Duvall, T. L. 1982, *Nature*, 300, 242
- Dziembowski, W. 1977, *AcA*, 27, 95
- Dziembowski, W. A. & Soszyński, I. 2010, *A&A*, 524, A88
- Dziembowski, W. A., Gough, D. O., Houdek, G. & Sienkiewicz, R. 2001, *MNRAS*, 328, 601
- Edmonds, P. D. & Gilliland, R. L. 1996, *ApJ*, 464, L157
- Fletcher, S. T., Chaplin, W. J., Elsworth, Y., Schou, J. & Buzasi, D. 2006, *MNRAS*, 371, 935
- Fontaine, G. & Brassard, P. 2008, *PASP*, 120, 1043
- Frandsen, S., Carrier, F., Aerts, C., Stello, D., Maas, T., et al. 2002, *A&A*, 394, L5
- Gai, N., Basu, S., Chaplin, W. J. & Elsworth, Y. 2011, *ApJ*, 730, 63
- Gilliland, R. L., Brown, T. M., Christensen-Dalsgaard, J., Kjeldsen, H., Aerts, C., et al. 2010, *PASP*, 122, 131
- Goldreich, P. & Keeley, D. A. 1977, *ApJ*, 212, 243
- Goldreich, P., Murray, N. & Kumar, P. 1994, *ApJ*, 424, 466
- Gough, D. O. 1977, *ApJ*, 214, 196
- Gough, D. O. 1980, in *Lecture Notes in Physics*, vol. 125, eds H. A. Hill & W. Dziembowski, Springer-Verlag, p. 273
- Gough, D. O. 1986, in *Hydrodynamic and magnetohydrodynamic problems in the Sun and stars*, ed. Y. Osaki, Department of Astronomy, University of Tokyo, p. 117
- Gough, D. O. 1990, in *Progress of seismology of the sun and stars, Lecture Notes in Physics*, vol. 367, eds Y. Osaki & H. Shibahashi, Springer, Berlin, p. 283
- Gough, D. O. 1993, in *Astrophysical fluid dynamics, Les Houches Session XLVII*, eds J.-P. Zahn & J. Zinn-Justin, Elsevier, Amsterdam, p. 399
- Gough, D. O. 2007, *AN*, 328, 273
- Grigahcène, A., Dupret, M.-A., Gabriel, M., Garrido, R. & Scuflaire, R., 2005. *A&A*, 434, 1055
- Hekker, S., Caerts, C., De Ridder, J. & Carrier, F. 2006, *A&A*, 458, 931
- Hekker, S., Gilliland, R. L., Elsworth, Y., Chaplin, W. J., De Ridder, J., Stello, D., Kallinger, T., Ibrahim, K. A., Klaus, T. C. & Li, J. 2011, *MNRAS*, in the press [[arXiv:1103.0141](#)]
- Houdek, G. 2010a, *AN*, 331, 998
- Houdek, G. 2010b, *Ap&SS*, 328, 237

- Houdek, G. & Gough, D. O. 2002, *MNRAS*, 336, L65
- Houdek, G. & Gough, D. O. 2007, *MNRAS*, 375, 861
- Houdek, G., Balmforth, N. J., Christensen-Dalsgaard, J. & Gough, D. O. 1999, *A&A*, 351, 582
- Huber, D., Bedding, T. R., Stello, D., Mosser, B., Mathur, S., et al. 2010, *ApJ*, 723, 1607
- Iglesias, C. A. & Rogers, F. J. 1996, *ApJ*, 464, 943
- Innis, J. L., Isaak, G. R., Brazier, R. I., Belmonte, J. A., Palle, P. L., Roca Cortes, T. & Jones, A. R. 1988, in *Seismology of the Sun & Sun-like Stars*, eds V. Domingo & E. J. Rolfe, ESA SP-286, ESA Publications Division, Noordwijk, The Netherlands, p. 569
- Kallinger, T., Weiss, W. W., Barban, C., Baudin, F., Cameron, C., Carrier, F., De Ridder, J., Goupil, M.-J., Gruberbauer, M., Hatzes, A., Hekker, S., Samadi, R. & Deleuil, M. 2010, *A&A*, 509, A77
- Kippenhahn, R. & Weigert, A. 1990, *Stellar structure and evolution*, Springer-Verlag, Berlin
- Kiss, L. L. & Bedding, T. R. 2003, *MNRAS*, 343, L79
- Kiss, L. L. & Bedding, T. R. 2004, *MNRAS*, 347, L83
- Kjeldsen, H. & Bedding, T. R. 1995, *A&A*, 293, 87
- Kjeldsen, H., Bedding, T. R. & Christensen-Dalsgaard, J. 2008, *ApJ*, 683, L175
- Kumar, P., Franklin, J. & Goldreich, P. 1988, *ApJ*, 328, 879
- Mazumdar, A. 2005, *A&A*, 441, 1079
- Miglio, A., Montalbán, J., Baudin, F., Eggenberger, P., Noels, A., Hekker, S., De Ridder, J., Weiss, W. & Baglin, A. 2009, *A&A*, 503, L21
- Miglio, A., Montalbán, J., Carrier, F., De Ridder, J., Mosser, B., Eggenberger, P., Scuflaire, R., Ventura, P., D'Antona, F., Noels, A. & Baglin, A. 2010, *A&A*, 520, L6
- Montalbán, J., Miglio, A., Noels, A., Scuflaire, R. & Ventura, P. 2010, *ApJ*, 721, L182
- Monteiro, M. J. P. F. G. & Thompson, M. J. 2005, *MNRAS*, 361, 1187
- Mosser, B., Belkacem, K., Goupil, M.-J., Miglio, A., Morel, T., Barban, C., Baudin, F., Hekker, S., Samadi, R., De Ridder, J., Weiss, W., Auvergne, M. & Baglin, A. 2010, *A&A*, 517, A22
- Mosser, B., Belkacem, K., Goupil, M. J., Michel, E., Elsworth, Y., et al. 2011a, *A&A*, 525, L9
- Mosser, B., Barban, C., Montalbán, J., Beck, P. G., Miglio, A., et al. 2011b, *A&A*, in the press [[arXiv:1105.6113v2](#)]
- Retter, A., Bedding, T. R., Buzasi, D. L., Kjeldsen, H. & Kiss, L. L. 2003, *ApJ*, 591, L151 (Erratum: *ApJ*, 596, L125)
- Rogers, F. J., Swenson, F. J. & Iglesias, C. A. 1996, *ApJ*, 456, 902
- Samadi, R., Georgobiani, D., Trampedach, R., Goupil, M. J., Stein, R. F. & Nordlund, Å. 2007, *A&A*, 463, 297
- Serenelli, A. & Weiss, A. 2005, *A&A*, 442, 1041
- Smith, P. H., McMillan, R. S. & Merline, W. J. 1987, *ApJ*, 317, L79
- Soszyński, I., Dziembowski, W. A., Udalski, A., Kubiak, M., Szymański, M. K., Pietrzyński, G., Wyrzykowski, L., Szewczyk, O. & Ulaczyk, K. 2007, *AcA*, 57, 201
- Stein, R. F. 1968, *ApJ*, 154, 297
- Stello, D., Bruntt, H., Preston, H. & Buzasi, D. 2008, *ApJ*, 674, L53
- Tabur, V., Bedding, T. R., Kiss, L. L., Giles, T., Derekas, A. & Moon, T. T. 2010, *MNRAS*, 409, 777
- Tassoul, M. 1980, *ApJS*, 43, 469
- Tassoul, M. 1990, *ApJ*, 358, 313
- Teixeira, T. C., Christensen-Dalsgaard, J., Carrier, F., Aerts, C., Frandsen, S., et al. 2003, *ApJSS*, 284, 233
- Unno, W. 1967, *PASJ*, 19, 140
- Vandakurov, Yu. V. 1967, *Astron. Zh.*, 44, 786 (English translation: *Soviet Astronomy AJ*, 11, 630)
- Vorontsov, S. V., Baturin, V. A. & Pamyatnykh, A. A. 1991, *Nature*, 349, 49
- Xiong, D. R., Chen, Q. L. & Deng, L. 1997, *ApJS*, 108, 529
- Xiong, D. R. & Deng, L. 2010, *MNRAS*, 405, 2759